Optics and Lasers in Engineering 108 (2018) 54–67

Contents lists available at ScienceDirect

Optics and Lasers in Engineering

journal homepage: www.elsevier.com/locate/optlaseng

Higher sensitivity Digital Gradient Sensing configurations for quantitative visualization of stress gradients in transparent solids

C. Miao, H.V. Tippur*

Department of Mechanical Engineering, Auburn University, AL 36849, United States

A B S T R A C T

Two modified full-field Digital Gradient Sensing (DGS) methods of higher measurement sensitivity relative to the prevailing ones are described for quantifying small angular deflections of light rays caused by stresses in transparent solids. These methods are devised by combining or altering previously proposed reflection-mode DGS (r-DGS) [1] and transmission-mode DGS (t-DGS) [2] methods. The concept involves increasing the optical path within the stressed medium by introducing an additional reflective surface behind the transparent solid, either as a separate reflector or as a rear surface reflective film deposition. The former approach is designated as t2-DGS method whose measurement sensitivity is twice that of t-DGS. The latter method results in an even higher sensitivity and is called the transmission-reflection DGS or tr-DGS method by making the back surface of a transparent planar solid reflective. The governing equations of tr-DGS are introduced first followed by a comparative demonstration of t2-DGS and tr-DGS methods by measuring the stress gradients in the crack-tip region during dynamic and static fracture experiments, respectively. Results show that tr-DGS is approx. 1.5 times more sensitive than t2-DGS, and at least three times more sensitive than t-DGS approach. Together as a family of DGS methods, these methods are used to extract the crack-tip stress intensity factors of PMMA beams under quasi-static loading conditions. The measured stress intensity factors are in good agreement with the predictions.

1. Introduction

Transparent materials are widely used in engineering applications such as aircraft canopies, automotive windshields, and electronic displays. Among them, transparent ceramics and glasses are popular due to many favorable characteristics namely low cost, high stiffness and scratch resistance, and very high compression strength, etc. Further, laminated glasses involving polymer films are used in transparent armor applications [3–5]. Understanding their failure mechanisms is critical for assuring mechanical integrity of structures which use them.

It is important to recognize that over the years several optical methods for full-field, non-contact measurement of deformations, strains and stresses have been proposed for dynamic failure characterization studies in solids. For example, photoelasticity has been used in conjunction with high-speed photography to measure in-plane maximum shear stresses [6,7] near dynamically growing cracks. Moiré interferometry has been used for dynamic fracture studies to measure in-plane displacement fields [8]. Measurement of stress gradients and surface slopes by a full-field lateral shearing interferometer called coherent gradient sensing (CGS) [9–11] has been another popular optical tool to evaluate dynamic fracture parameters. Recently, novel phase shifting approaches to CGS have been proposed to quantify surface slopes accurately [12,13]. In all these methods, optical fringes are typically recorded in real time. These methods also require special optical characteristics of the material (e.g., birefringence) or surface preparation (e.g., deposition of gratings), and/or specialized optics for implementation. Hence, vision-based full-field methods such as Digital Image Correlation (DIC) have become popular in recent years for measuring surface deformations [14–17]. The attractive features of these techniques including the simplicity of surface preparation, ordinary white light illumination, and feasibility of 2D or 3D measurements make DIC rather prevalent as an optical metrology tool in experimental mechanics. In its wake, a new full-field optical method called Digital Gradient Sensing (DGS) was proposed by Periasamy and Tippur for measuring two orthogonal angular deflections of light rays caused by stresses in transparent solids [2,18]. Subsequently, DGS was modified to study opaque, optically reflective objects to measure orthogonal surface slopes [1]. The simplicity of the experimental setup and its high measurement sensitivity make DGS attractive for experimental mechanics investigations. Furthermore, it has been shown that these measured quantities can be numerically integrated to evaluate surface profiles or stress fields with high fidelity. Miao et al. [19] investigated the feasibility of reflection-mode DGS (r-DGS) in conjunction with a robust higher-order finite-difference-based least-squares integration (or simply HFLI) scheme to measure the surface topography of thin structures. Zhang et al. adopted DGS to measure thermal deformations in transparent objects at elevated temperatures [20]. Recently, Sundaram and Tippur studied fracture mechanics of transparent soda-lime glass by using transmission mode DGS or t-DGS [21,22]. As noted in [22], due to its low fracture toughness and high stiffness, the non-singular crack-tip deformations are extremely challenging to evaluate in transparent ceramics because deformations are confined to an extremely small region near an almost ‘mathematically sharp’ crack-tip. This makes implementation of traditional DIC difficult to fast fracture studies in such materials, relative to DGS which uses an ‘optical lever/arm’ for amplifying the effects of the singular stress fields. That is, measurement sensitivity of DGS can be increased by increasing the distance between the specimen and the speckle target. Though it is conceptually straight forward, this idea poses subtle and significant implementation challenges including

* Corresponding author.
E-mail address: tippuhv@auburn.edu (H.V. Tippur).

https://doi.org/10.1016/j.optlaseng.2018.04.005
Received 17 January 2018; Received in revised form 17 March 2018; Accepted 3 April 2018

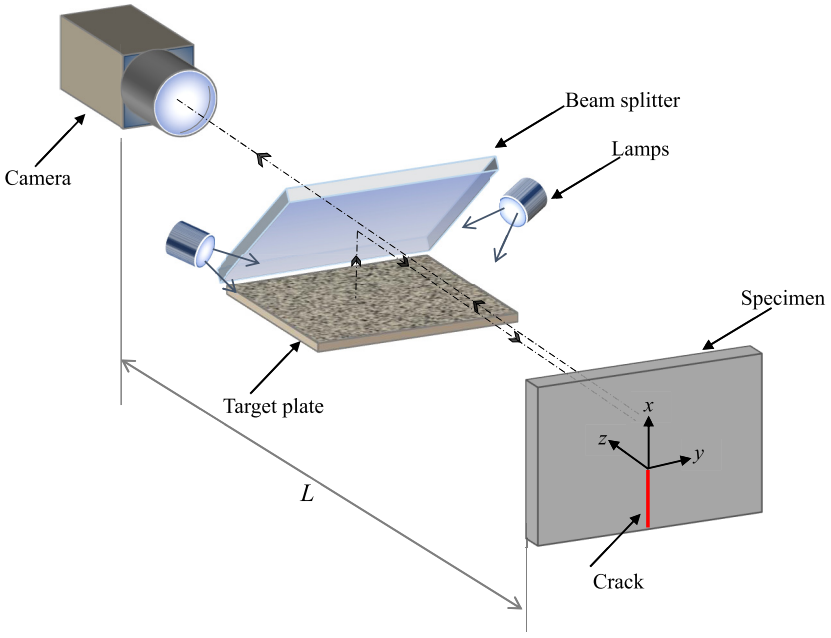

Fig. 1. Schematic of experimental setup for reflection DGS (r-DGS). (Setups for t2-DGS and tr-DGS are similar to r-DGS, see text for details). (For interpretation of the references to color in the figure text, the reader is referred to the web version of this article.)

insufficient light to expose the sensor during dynamic events and vibration isolation requirements during slow/quasi-static events. Hence, DGS methods of higher measurement sensitivity without needing significant increase of 'optical arm' are attractive. In this context, two modified DGS methods devised by combining or altering r-DGS and t-DGS methods in order to achieve this goal are presented here.

In the following, first the working principles of both r-DGS and t-DGS are briefly reviewed before introducing concepts for the two modified DGS methods and their respective governing equations. Then, these two new ideas are verified by measuring the stress gradients in the crack-tip region during dynamic and static fracture experiments, respectively. Subsequently, as a family of DGS methods, all the four techniques are used individually to extract the mode-I stress intensity factors relative to the theoretical counterpart in a problem of common fracture mechanics interest. Finally, the major results of this research are summarized.

2. Working principles of r-DGS and t-DGS

2.1. Reflection-mode Digital Gradient Sensing (r-DGS)

A schematic of the experimental setup for reflection-mode Digital Gradient Sensing (or r-DGS) to measure surface slopes is shown in Fig. 1. A digital camera is used to record random speckles on a target plane via the reflective specimen surface. To achieve this, the specimen and the target plate are placed perpendicular to each other, and the beam splitter is placed at 45° relative to the specimen and target plate, respectively.[1] The target plate is coated with random black and white spray painted speckles, and is illuminated uniformly using a broad spectrum white light. The specimen surface is made reflective (Fig. 2(a)) using vapor deposition of aluminum film or using the film transfer technique [23]. (The front face of the specimen illustrated in Fig. 2 is towards to the camera and the target plate.) When the specimen is in the undeformed state, the gray scale at a generic point P on the target plate

[1] An additively printed beam splitter holder with a random speckle coated planar baseplate is used to accomplish the optical alignment.

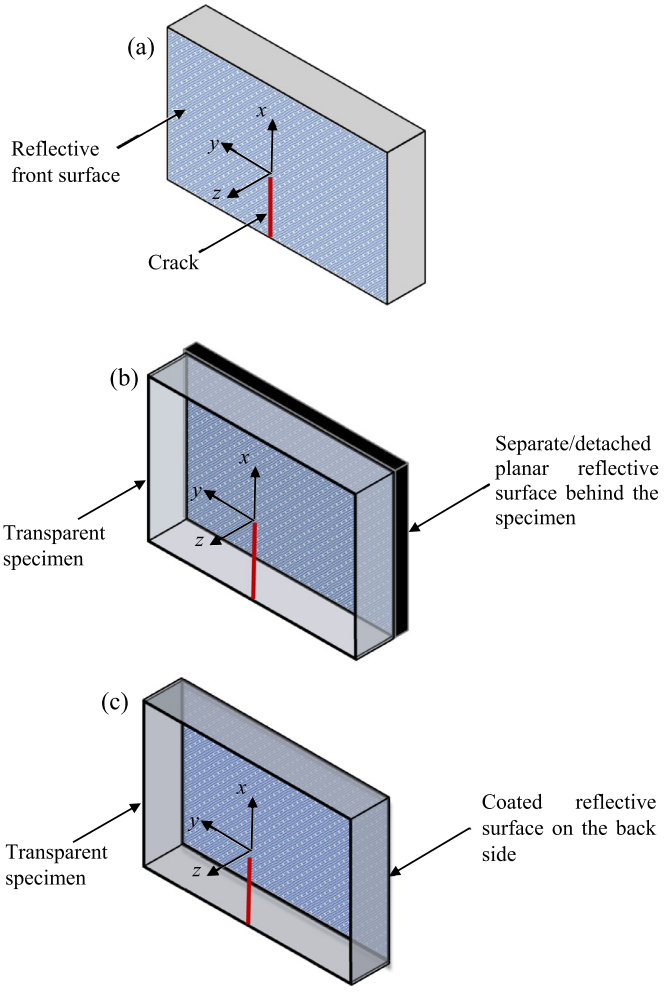

Fig. 2. Specimen configurations for: (a) r-DGS; (b) t2-DGS; (c) tr-DGS.

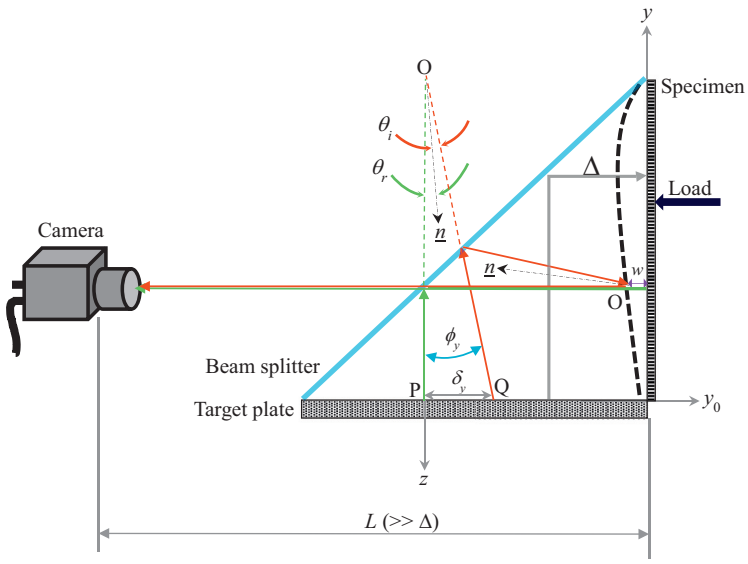

Fig. 3. Working principle of r-DGS [19].

is photographed by a camera pixel through point O on the specimen plane. Thus recorded image at that time instant and/or load level is the reference image. After the specimen suffers deformation, say, due to the applied load, the gray scale at a neighboring point of P, namely S on the target plate is photographed by the same pixel through the same point O on the specimen surface. The corresponding image of the specimen in the deformed state is recorded next. The local orthogonal speckle displacements $\delta_{y:x}$ can be obtained by performing a 2D image correlation of the reference and deformed images. The corresponding angles $\phi_{x:y}$ representing two orthogonal angular deflections of light rays can then be obtained as shown in the schematic Fig. 3.

For simplicity, only the angular deflections of light rays in the y–z plane are shown in Fig. 3. Here, OP makes an angle ϕ_y with OQ. Further, $\phi_y = \theta_i + \theta_r$ where θ_i and $\theta_r(=\theta_i)$ are incident and reflected angles relative to the normal to the specimen. A similar relationship in the x–z plane can be obtained as well. Then, the two orthogonal surface slopes of the surface can be related to $\phi_{y:x}$ as $\frac{\partial w}{\partial y:x} = \frac{1}{2}\tan(\phi_{y:x})$. The governing equations for r-DGS thus are [1]

$$\frac{\partial w}{\partial y:x} = \frac{1}{2}\tan\left(\phi_{y:x}\right) \approx \frac{1}{2}\left(\phi_{y:x}\right) \approx \frac{1}{2}\left(\frac{\delta_{y:x}}{\Delta}\right) \tag{1}$$

where Δ is the distance or the gap between the specimen and target planes. It is important to note that the coordinates of the specimen plane are utilized for describing the governing equations and the camera is focused on the target plane during photography. Therefore, a coordinate mapping is needed to transfer the target plane locations to the specimen plane. This can be done using the pin-hole camera approximation, $(x:y) = \frac{L}{L+\Delta}(x_0:y_0)$, where $(x:y)$ and $(x_0:y_0)$ represent the coordinates of the specimen and target planes, respectively, and L is the distance between the specimen and the camera [2].

2.2. Transmission-mode Digital Gradient Sensing (t-DGS)

A schematic of the experimental setup for transmission-mode Digital Gradient Sensing (t-DGS) method is shown in Fig. 4(a). Unlike in the r-DGS setup, a random speckle pattern on the target plate is recorded through a transparent specimen in t-DGS. As in r-DGS, a reference image is recorded first. That is, the gray level at point P on the target plane corresponding to point O on the specimen plane is recorded initially. The refractive index and thickness of the specimen change after imposing a load on the specimen. As a result, the light rays deviate from their

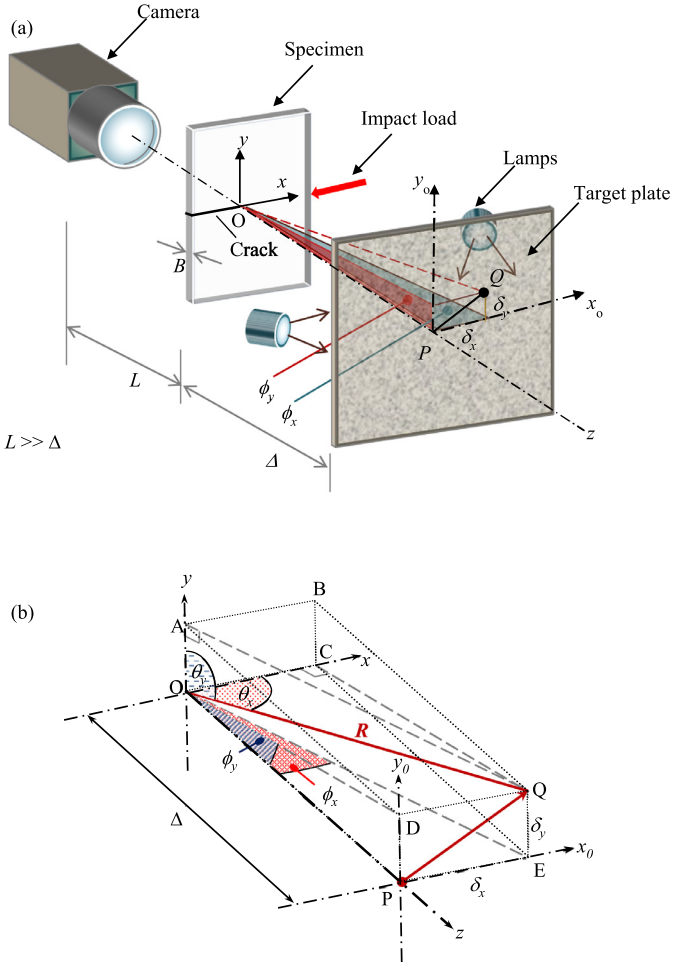

Fig. 4. Schematic of experimental setup (a) and working principle (b) for t-DGS [2].

initial path due to the so-called elasto-optical effect. In the deformed state of the specimen, another image is recorded with the gray scale at a neighboring point of P, namely Q, on the target plane, recorded by the same pixel through O on the specimen plane. The local speckle displacements $\delta_{x:y}$ can be quantified by correlating the reference image with the deformed image of the specimen. The angles $\phi_{x:y}$ are the two orthogonal angular deflections of light rays, and can be explained as follows:

The optical path change, δS, between the original light ray OP and deflected light ray OQ caused by the deformation of the specimen, can be expressed as [10]:

$$\delta S(x,y) = 2B(n-1)\int_0^{1/2} \varepsilon_{zz}\, d(z/B) + 2B\int_0^{1/2} \delta n\, d(z/B) \tag{2}$$

The two integrals on the right hand side of the above equation represent the contributions of the normal strain in the thickness direction, ε_{zz}, and the change in the refractive index, δn, to the overall optical path, respectively. The Maxwell-Neumann relationship [24] states that the refractive index change is proportional to the local state of normal stresses in the specimen. The strain, ε_{zz}, can be related to the normal stresses using the generalized Hooke's law for an isotropic, linear elastic solid. Thus, for plane stress conditions, Eq. (2) reduces to [2],

$$\delta S(x,y) = C_\sigma B(\sigma_{xx} + \sigma_{yy}) \tag{3}$$

where $C_\sigma = D_1 - (\upsilon/E)(n-1)$ is the elasto-optic constant of the specimen material.

The deflected light ray OQ make solid angles θ_x and θ_y with the x- and y-axes, respectively, as shown in Fig. 4(b). It is evident from the above equations that, for small angular deflections, the direction cosines of OQ, $\cos\theta_{x:y}$, are related to the in-plane stress gradients as,

$$\cos\theta_{x:y} = \frac{\partial(\delta S)}{\partial(x:y)} = C_\sigma B\frac{\partial(\sigma_{xx}+\sigma_{yy})}{\partial(x:y)} \tag{4}$$

Referring to the planes defined by points OAQ and OCQ shown in Fig. 4(b),

$$\cos\theta_{x:y} = \frac{\delta_{x:y}}{R} \tag{5}$$

where $R\ (=\sqrt{\Delta^2+\delta_x^2+\delta_y^2})$ is the distance between points O and Q, Δ is the distance between the specimen and target planes. For small angular deflections, or $\delta_{x:y} \ll \Delta$, the two angular deflections of light rays, $\phi_{x:y}$, are related to the in-plane stress gradients as [2],

$$\phi_{x:y} \approx \frac{\delta_{x:y}}{\Delta} \approx \cos\theta_{x:y} = C_\sigma B\frac{\partial(\sigma_{xx}+\sigma_{yy})}{\partial(x:y)} \tag{6}$$

Again, as in r-DGS, the pin-hole camera mapping function needs to be used here to transfer the coordinates of the target plane to the specimen plane.

3. Extensions to r-DGS and t-DGS

3.1. Double/Dual transmission Digital Gradient Sensing (t2-DGS)

A schematic of experimental setup for double transmission (or, dual transmission) Digital Gradient Sensing or simply t2-DGS method is similar to the one shown in Fig. 1. That is, it is similar to the setup for r-DGS (Fig. 2(a)) except a separate/detached reflective planar surface is placed flush with the specimen on its backside, as shown in Fig. 2(b). (That is, the gap between the additional reflective surface and the rear surface of the specimen is nominally zero.) The light rays, originating from the target plane, pass through the transparent specimen and reach the reflective surface and then get reflected back into the transparent specimen. Hence, the speckles on the target are recorded by the camera via the additional reflective surface. As in r-DGS, a reference image is recorded first and then the deformed images as the specimen is subjected to load. The local displacements $\delta_{x:y}$ can be measured by correlating the reference image with the deformed images. Thus, light rays experience the elasto-optical effects over twice the specimen thickness as a result of retro-reflection immediately after leaving the rear face. Hence, the optical path change here is twice that of t-DGS,

$$\delta S_{t2-DGS} = 2\left(\delta S_{t-DGS}\right) \tag{7}$$

The two angular deflections of light rays of t2-DGS $(\phi_{x:y})_{t2-DGS}$, which are related to the in-plane stress gradients, can be then be expressed as:

$$(\phi_{x:y})_{t2-DGS} = 2(\phi_{x:y})_{t-DGS} = 2C_\sigma B\frac{\partial(\sigma_{xx}+\sigma_{yy})}{\partial(x:y)} \tag{8}$$

From the above, it is evident that the sensitivity of t2-DGS is twice that of t-DGS.

A 2D ray diagram, Fig. 5(a) is used to depict the path a light ray would take through a deformed specimen in the t2-DGS methodology. The above Eq. (8) assumes that the specimen is 'thin' or 'stiff' or both such that the incident and reflected light rays have a negligibly small lateral shift (OO') between them. The exaggerated ray diagram depicts the light path through the specimen for clarity. An incident ray enters the deformed specimen (shaded in blue) and refracts at point 'a'. Then, it continues to bend progressively[2] as it propagates through-the-thickness due to continuous local refractive index changes, and exits the deformed specimen at point 'b'. Next, it reflects off the detached reflector at point 'c', enters the deformed specimen again and refracts at point 'd'. After a second transmission through the sample thickness, it exits the specimen at point 'e'. In t-DGS, the angular deflection is assumed to occur at point O along the centerline of the specimen instead of 'a' or 'b' after all the refraction and thickness changes are lumped together. In t2-DGS, however, the ray reflected off the rear surface reflector passes through O' during the second transmission. The distance OO' is assumed to be negligible in the analysis. Obviously, if the detached reflective surface is not kept flush with the specimen, parallelism of the reflector relative to the undeformed specimen cannot be assured and additional errors could occur.

3.2. Transmission-Reflection Digital Gradient Sensing (tr-DGS)

The schematic of the experimental setup for transmission-reflection Digital Gradient Sensing (tr-DGS) method is again similar to the one shown in Fig. 1. Furthermore, the experimental setup for tr-DGS is similar to the one for t2-DGS. However, in tr-DGS, the specimen is transparent but its rear face is made reflective by a reflective film deposition, as shown in Fig. 2(c). The light rays, originating from the target plane, pass through the transparent specimen and then get reflected by the rear surface. The reflected rays then propagate through the transparent specimen for the second time. As in other DGS methods, a reference image is recorded first followed by images in the deformed state of the specimen. That is, gray scale at point P on the target plate which corresponds to point O on the specimen plane is recorded. In addition to the refractive index and thickness changes of the specimen, in this case the reflective rear surface of the specimen also deforms due to stress. As a result of these combined effects, light rays deviate from their initial path. In the deformed state of the specimen, an image is recorded. That is, the gray scale at a neighboring point of P, namely Q on the target plane, is recorded through O on the specimen plane. As before, the local speckle displacements $\delta_{x:y}$ can be quantified by correlating the reference image with the deformed image of the specimen.

In r-DGS, the reflective surface deforms when the specimen is stressed. In t2-DGS, the refractive index and thickness of the specimen change when the specimen is stressed. The tr-DGS method combines r-DGS and t2-DGS. That is, in tr-DGS, the refractive index and thickness of the specimen change, and the reflective rear surface of specimen also

[2] considered here as a straight line for depiction and simplicity of analysis.

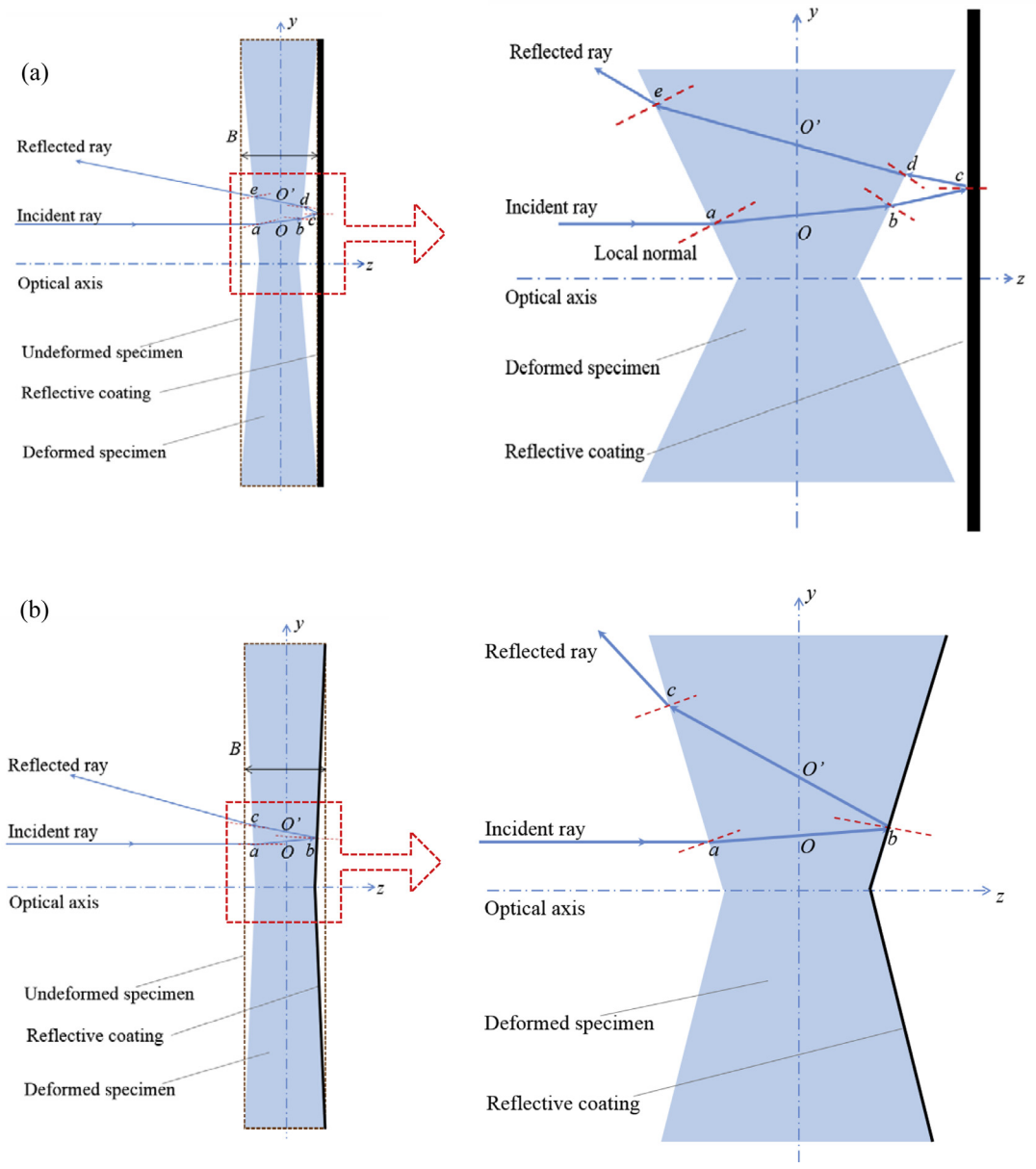

Fig. 5. Light ray diagrams for t2-DGS (a) and tr-DGS (b).

deforms when the specimen is stressed, which makes tr-DGS more sensitive for the same stress field as these effects are additive in nature. Hence, the angular deflections of light rays of tr-DGS $(\phi_{x:y})_{tr-DGS}$ is a combination of r-DGS $(\phi_{x:y})_{r-DGS}$ and t2-DGS $(\phi_{x:y})_{t2-DGS}$,

$$(\phi_{x:y})_{tr-DGS} = \frac{\delta_{x:y}}{\Delta} = (\phi_{x:y})_{r-DGS} + (\phi_{x:y})_{t2-DGS} \tag{9}$$

As noted earlier,

$$(\phi_{x:y})_{r-DGS} = 2\frac{\partial w}{\partial(x:y)} \tag{10}$$

and for plane stress, $\varepsilon_{zz} \approx \frac{2w}{B} = -\frac{\upsilon}{E}(\sigma_{xx} + \sigma_{yy})$, and hence

$$w \approx -\frac{\upsilon B}{2E}(\sigma_{xx} + \sigma_{yy}) \tag{11}$$

where υ is the Poisson's ratio, B is the undeformed thickness, and E is the elastic modulus of the specimen. Hence, Eq. (9) can be written as,

$$(\phi_{x:y})_{tr-DGS} = \frac{\delta_{x:y}}{\Delta} = \left(2C_\sigma B - \frac{\upsilon B}{E}\right)\frac{\partial(\sigma_{xx} + \sigma_{yy})}{\partial(x:y)} \tag{12}$$

As in t2-DGS, the above Eq. (12) assumes that the specimen is 'thin' or 'stiff' or both such that the incident and reflected light rays have negligible lateral shift (OO'), see Fig. 5(b), between them. A ray diagram is shown in Fig. 5(b) to track the bending of a generic light ray through the specimen. An incident ray enters the deformed specimen (shaded in blue) and refracts at point 'a'. Then, it continues to bend progressively (shown as straight lines for simplicity of depiction and analysis) as it propagates through-the-thickness due to refractive index changes. Next, it reflects off the deformed rear specular surface at point 'b' according to the laws of reflection and reenters the specimen. At last, it exits the specimen after refraction at point 'c'. As in t2-DGS, the distance of OO' can be negligible when the specimen is 'thin' or 'stiff' or both. The value of OO' is estimated in Appendix-A with the above simplified assumptions.

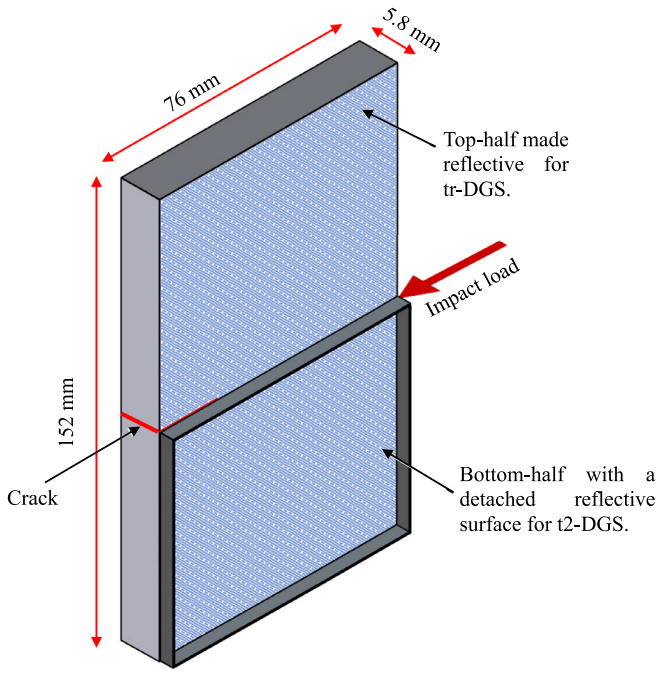

Fig. 6. Back-side of the specimen with and without reflective coating in the upper-half and lower-half, respectively. (Front-side of the specimen faces the camera).

4. Experimental verification

4.1. Dynamic[3] fracture experiment

The working principle for t2-DGS is relatively straightforward and hence a separate verification for t2-DGS is deemed unnecessary. Instead, a comparative evaluation of tr-DGS method with t2-DGS is carried out. A cracked PMMA plate undergoing dynamic mode-I fracture is used for this demonstration in which stress gradients in the crack-tip region are measured from the two methods relative to each other. A 152 mm × 76 mm rectangular specimen of 5.8 mm thickness was imaged using ultrahigh-speed digital camera having a single imaging sensor. The specimen configuration as viewed from its backside is shown in Fig. 6 with its front surface facing the camera. A 10 mm long horizontal pre-notch was cut along the edge in the mid-span of the specimen using a 300 μm thick diamond saw. The top-half of the backside of the specimen was deposited with a thin aluminum film to make it reflective to implement tr-DGS. In the bottom-half, a reflective planar surface (mirror) was placed flush with the specimen for implementing t2-DGS. The cracked specimen was subjected to symmetric mode-I loading by impacting it on the uncracked long-edge. Thus, during the experiment, stress gradients were measured simultaneously by tr-DGS and t2-DGS methods in the upper- and lower-halves on the same specimen with a mode-I crack subjected to the same stress field. The relevant properties of PMMA used in this experiment are listed in Table. 1.

Table 1
Material properties of PMMA [2,18].

	Dynamic	Static
Density (kg/m^3)	1100	1100
Elastic modulus (GPa)	4.92	3.30
Poisson's ratio	0.34	0.34
Elasto-optic constant (m^2/N)	-1.08×10^{-10}	-0.90×10^{-10}

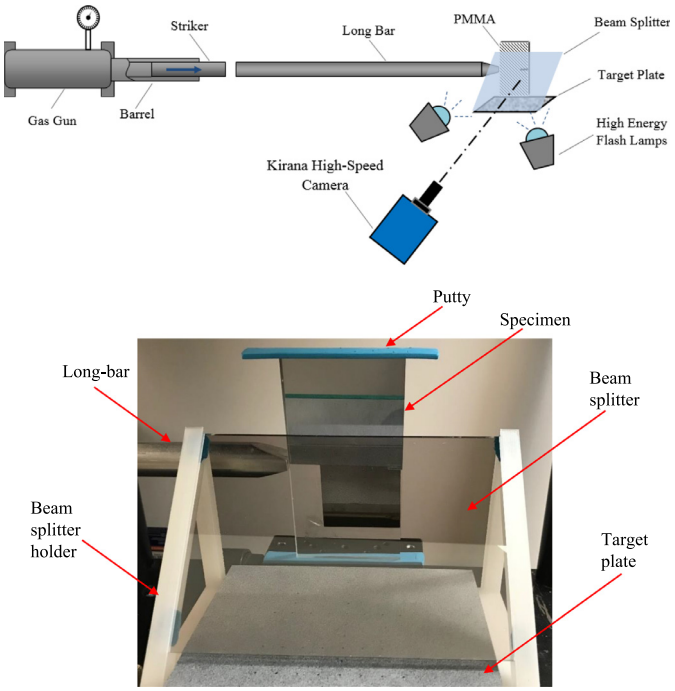

Fig. 7. Schematic (top) and close-up photography (bottom) of the experimental setup for dynamic plate impact study.

The schematic of the overall experimental setup used for the dynamic impact experiment is shown in Fig. 7. A modified Hopkinson pressure bar (or simply a 'long-bar') was used for loading the specimen using stress waves. The long-bar was a 1.83 m aluminum rod of 25.4 mm diameter with a tapered rectangular tip (25.4 mm × 7.5 mm) impacting the unconstrained PMMA plate. A 305 mm long, 25.4 mm diameter aluminum striker placed in the barrel of a gas-gun was aligned co-axially with the long-bar at the start of the experiment. The striker was launched towards the long-bar at a velocity of ~13 m/s during the test. A close-up view of the optical arrangement is also shown in Fig. 7. Initially, the long-bar was kept in contact with the specimen. The specimen was placed over a rectangular strip of soft putty stuck to a height-adjustable aluminum platform to prevent direct contact with the platform and simulate a 'free-standing' specimen configuration. To achieve symmetry in terms of acoustic impedance, a separate putty strip was pressed onto the top edge of the specimen. As noted earlier, the top-half of the backside of the specimen is coated with aluminum film to make it specular. And, a reflective planar mirror was placed flush with the bottom-half. A beam splitter and the speckle target plate were placed in a specially designed 45° holder so that the camera could be focused on the speckles through the beam splitter via the specimen. The speckle images were photographed by a Kirana-05 M ultrahigh-speed digital camera assisted by a pair of Cordin-659 high energy flash lamps to illuminate the speckles on the target. The camera is a single sensor camera capable of recording 10-bit gray scale images at a maximum rate of 5 million frames per second and at a fixed spatial resolution of 924 × 768 pixels per image.

[3] It is rather traditional to perform quasi-static experiments before conducting dynamic counterparts for establishing a new experimental method. When using speckle-based methods, however, the possibility of rigid body motions exists during quasi-static loading events lasting relatively long duration (a few seconds or more). Such issues, on the other hand, are negligible if not completely absent during stress-wave dominant loading events lasting only a few microseconds *and* speckle images being recorded using a single sensor ultrahigh-speed camera (without any moving parts) where both the reference and deformed images are a few microseconds apart and recorded by the same sensor, thus limiting recording issues to the electronic noise. Hence, a dynamic experiment is favored for this demonstration to a quasi-static counterpart to address the primary issue of measurement sensitivity between methods.

The camera and the two flash lamps were triggered using a variable delay circuit relative to the striker impacting the long-bar and knowing the duration required for the stress waves to travel the length of the long-bar.

A Nikon 70–300 mm focal length macro zoom lens and adjustable bellows was used with the camera to record the images. A good depth-of-focus over the entire field was achieved by stopping down the lens aperture to F# 11.0 after focusing on the speckles. The distance between the specimen and the camera lens plane (L) was ~795 mm and the one between the specimen mid-plane and the target plane (Δ) was 72 mm. The camera was focused on a rectangular region of interest (ROI) approximately 40 mm × 35 mm on the specimen plane in the vicinity of the pre-notch tip. When the long-bar was impacted by the striker, a compressive stress wave generated in the long-bar propagated along its length. Simultaneously a trigger pulse was generated to start recording of images by the camera. A total of 180 images, some corresponding to the undeformed state and others to the deformed state of the specimen, were recorded at 400 K frames per second (inter frame period 2.5 μs). One of the undeformed images before the start of loading pulse entering the specimen was selected as the reference image. All the deformed images were correlated with that reference image using ARAMIS® image analysis software. During image correlation, a sub-image size of 20 × 20 pixels (1 pixel = 48.30 μm) with 10 pixels overlap was used to extract the local speckle displacements $\delta_{x:y}$ in the ROI. The displacement fields were then used to compute the two orthogonal angular deflection fields of light rays ($\phi_{x:y}$) as detailed earlier.

The time-resolved angular deflection contour plots of $\phi_{x:y}$ in the PMMA plate are shown in Fig. 8 at a few select time instants. In these plots, t = 0 μs corresponds to crack initiation at the original notch tip. Both ϕ_x and ϕ_y contours increase in number and become denser with the passage of time implying buildup of stresses in the specimen during impact loading event. In each contour plot, the ones in the top-half are measured by tr-DGS and the bottom-half by t2-DGS methods. The boundary of these two is along the path of mode-I crack growth (or, along the x-axis). If only one of the two methods were used, the ϕ_x contours should be symmetric in shape and magnitude with respect to the crack whereas the ϕ_y contours should be symmetric in shape and anti-symmetric in magnitude. In the current implementation, however, the contours of $\phi_{x:y}$ are not symmetric due to the different measurement sensitivities of these two methods. It can be observed that the contours in the top-half measured by tr-DGS are denser and larger than those in the bottom-half measured by t2-DGS, indicating qualitatively that tr-DGS is more sensitive than t2-DGS. In the case of ϕ_x contours at t = 15 μs, the contour lines close to the left hand edge cluster due to the impact occurring over a narrow area of contact. Furthermore, the contours resulting from the impact waves are not as dominant in the t2-DGS method while they are rather pronounced in the top-half of the plot. It should be noted here that, although the $\phi_{x:y}$ contours are different in the top and bottom halves near the crack-tip, they are due to the same stress field. Hence, the values of $\phi_{x:y}$ along any symmetric angular paths with respect to the crack-tip polar coordinates ($\pm\theta$), measured by tr-DGS and t2-DGS, can be extracted to directly compare the sensitivities of these two methods.

Theoretically, the ratio of values of $\phi_{x:y}$ measured by tr-DGS and t2-DGS, based on Eqs. (8) and (12), can be written as:

$$\frac{(\phi_{x:y})_{tr-DGS}}{(\phi_{x:y})_{t2-DGS}} = \left(1 - \frac{\upsilon}{2C_\sigma E}\right) \tag{13}$$

It is evident that this ratio is dependent only on the properties of the specimen material. Based on the properties of PMMA listed in Table. 1, the result of Eq. (13) in the dynamic loading case should be ~1.32 whereas ~1.57 for quasi-static loading conditions due to the value of C_σ reported from different sources in the literature [25]. In the region around the crack-tip, discrete angular deflection values of $\phi_{x:y}$ along 45° and 90° paths in the range $0.5 \le r/B \le 1.5$ were considered. That is, $(\phi_{x:y})_{tr-DGS}$ along −45° and −90°, and $(\phi_{x:y})_{t2-DGS}$ along +45° and +90°, were extracted for comparison. (*It should be noted that the choice of these directions allowed direct use of measured angular deflections without further data interpolation since the shape of the sub-images used during image correlation were squares. Other angles, say, ±60° would require interpolation of sub-image data array and hence avoided.*) The choice of the radial extent ensured that the data was sufficiently close to the crack-tip to capture the singular behavior while minimizing triaxial effects [10] and any uncertainty of locating the origin due to a combination of limited optical aperture, loss of speckle correlation, and edge-effects. The details of the data paths are shown in Fig. 8(f). The red dot represents the crack-tip, r is the radial distance from the origin and the heavy black line represents the crack. It can be observed in the ϕ_y plot, the sign of the angular deflection values are opposite with respect to the growing crack path and hence, the values of $\frac{(\phi_y)_{tr-DGS}}{(\phi_y)_{t2-DGS}}$ are negative, while the values of $\frac{(\phi_x)_{tr-DGS}}{(\phi_x)_{t2-DGS}}$ are positive.

The experimental results of $\frac{(\phi_{x:y})_{tr-DGS}}{(\phi_{x:y})_{t2-DGS}}$ in $0.5 \le r/B \le 1.5$ range along ±45° and ±90° are shown in Fig. 9(a) and (b), respectively, at a few select time instants corresponding to the plots in Fig. 8. The blue theoretical band represents the range −1.57 to −1.32, and the yellow one represents the range 1.32–1.57. Ratios at $t = \pm 2.5$ μs indicate the experimental results just before and after crack initiation at $t = 0$ μs. Three consecutive time instants are selected here as typical examples for comparison. It can be observed from Fig. 9 that the data points at these time instants are nearly constant and close to the prediction. (The values of three data points of $t = 15$ μs within $0.5 \le r/B \le 0.7$ in Fig. 9(b) are zero because $(\phi_{x:y})_{tr-DGS}$ in that region are zero due to missing data around the crack-tip at $t = 15$ μs.) It is worth noting that, during analysis, sufficient care was exercised to locate the crack-tip.

Mode-I stress intensity factor (SIF) histories were evaluated using an over-deterministic least-squares analysis based on the angular deflections fields of (ϕ_x) measured by tr-DGS and t2-DGS methods,

$$\phi_x(t) = D\left[\begin{array}{l} -\frac{1}{2} r_l^{-\frac{3}{2}} \left\{ f(V; C_L; C_S) A_1(t) cos\left(\frac{3\theta_l}{2}\right)\right\} \\ + \sum_{N=2}^{\infty} \left\{ A_N(t)\left(\frac{N}{2} - 1\right) r_l^{\left(\frac{N}{2}-2\right)} cos\left(\left(\frac{N}{2} - 2\right)\theta_l\right)\right\} \end{array}\right] \tag{14}$$

where the constant D varies for each of the DGS methods, $D_{t2-DGS} = (2C_\sigma B)$ and $D_{tr-DGS} = (2C_\sigma B - \frac{\upsilon B}{E})$, f is a function of instantaneous crack velocity, V, (r_l, θ_l) denote the contracted crack tip polar coordinates for a growing crack (See [19] for details). Mode-I SIFs $K_I(t)$ are related to $A_1(t)$, as $A_1(t) = K_I(t)\sqrt{2/\pi}$. The values of ($\phi_x$) measured by tr-DGS and t2-DGS were used to calculate SIFs, respectively, the corresponding SIF histories are plotted in Fig. 10. It can be observed that two SIF histories match well with each other.

4.2. Static fracture experiment

To further demonstrate the validity of tr-DGS and t2-DGS methods for mechanics problems in general, a PMMA beam subjected to a symmetric 3-point bending was considered. A schematic of the experimental setup along with a companion photograph is shown in Fig. 11. A 152 mm × 51 mm rectangular PMMA specimen of 5.8 mm thickness, with an initial crack of length 13 mm was used. An Instron 4465 universal testing machine operating in displacement controlled mode (cross-head speed = 0.004 mm/s) was employed to load the specimen supported on two anvils (span 127 mm). In Fig. 11, the back side of the specimen on its right-half was deposited with a thin aluminum film to make it reflective for implementing tr-DGS. The left-half had a reflective planar surface kept flush against the specimen for t2-DGS implementation. Thus, during the experiment, stress gradients were measured by tr-DGS and t2-DGS methods simultaneously on the same specimen. A beam splitter and the speckle target plate were placed in a specially designed 45° holder, with the camera focused on the speckles through the beam splitter and via the specimen. The target plate was illuminated uniformly by two LED lamps. The distance (Δ) between the specimen mid-plane and the target plate was 80 mm. A Nikon D100 digital SLR

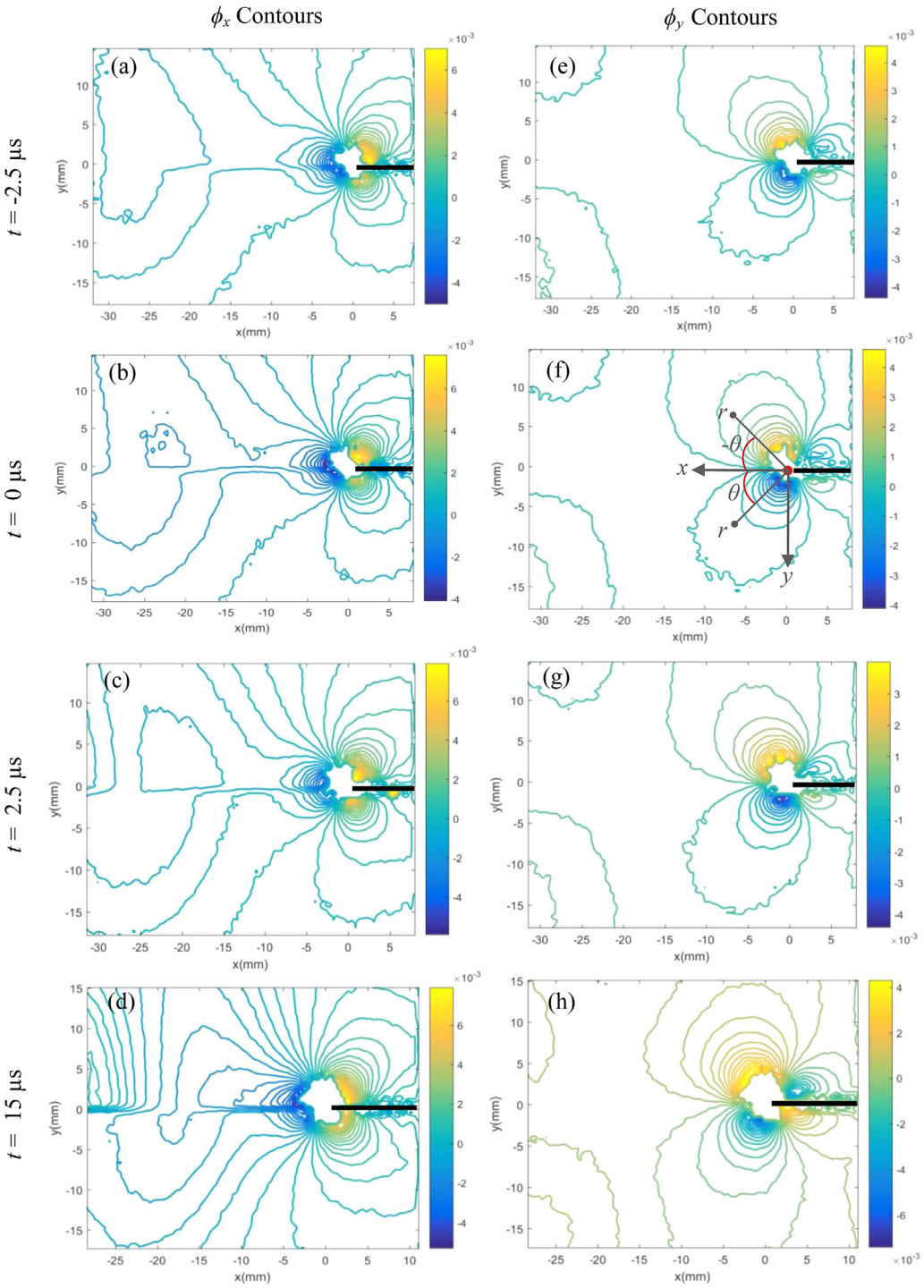

Fig. 8. Angular deflection contour plots proportional to stress gradients of $(\sigma_x + \sigma_y)$ in the x- and y-directions. Contour increments = 3×10^{-4} rad.

camera fitted with a 70–300 mm macro lens and an adjustable bellows was placed in-front of the specimen at a distance of 1350 mm (L). An aperture setting of $F^{\#}$ 11 was selected for recording the speckles with a good depth-of-focus. A computer was used to control both the camera and the loading devise during time-lapse photography of speckles.

An 8-bit reference image was recorded with a resolution of 1504×1000 pixels before loading the beam ($F = 0$ N). Subsequently, speckle images were recorded at every 50 N increments up to 300 N. The rigid body motion of speckles in the images was visible in the first increment. To minimize the effect of such motions on the experimental result, the image at $F = 100$ N was intentionally selected as the reference image. The one at $F = 300$ N was correlated with the reference image by using ARAMIS® image analysis software. During image correlation, a sub-image size of 20×20 pixels (1 pixel = 38.56 µm) with 10 pixels of overlap was used to extract the local speckle displacements $\delta_{x:y}$ in the ROI. The displacement fields were then used to compute the two orthogonal angular deflection fields of light rays $\phi_{x:y}$.

The angular deflection contour plots $\phi_{x:y}$ in the PMMA plate are shown in Fig. 12(a) and (b). In each contour plot, the left-half are from tr-DGS and the right-half are from t2-DGS. Similar to the dynamic experiments, it can be observed that the left-half contours are denser and larger in size than the right-half counterparts, indicating higher sensi-

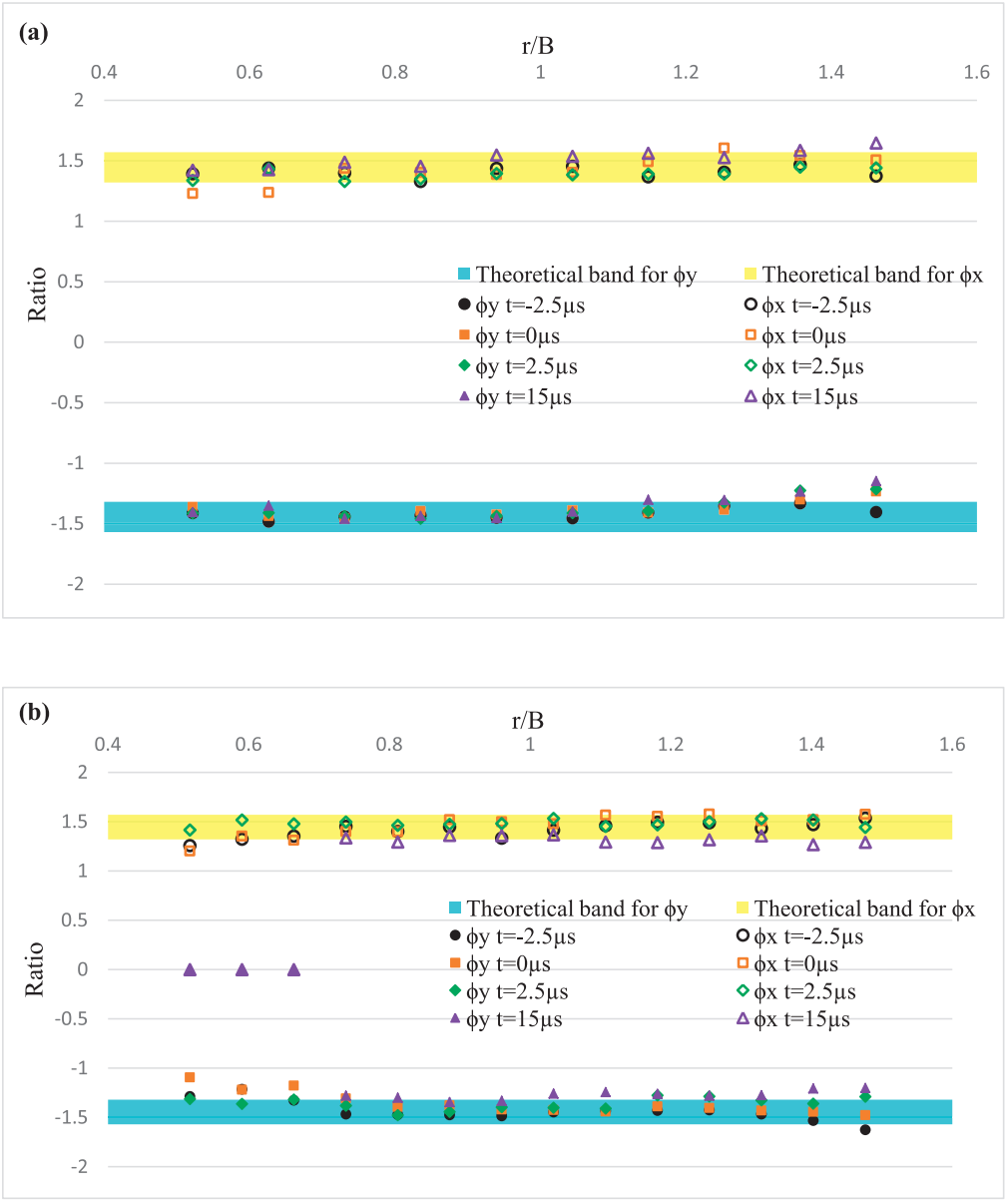

Fig. 9. Ratio of $\frac{(\phi_{x:y})_{tr-DGS}}{(\phi_{x:y})_{t2-DGS}}$ within $0.5 \le r/B \le 1.5$: (a) along ±45°; (b) along ±90°.

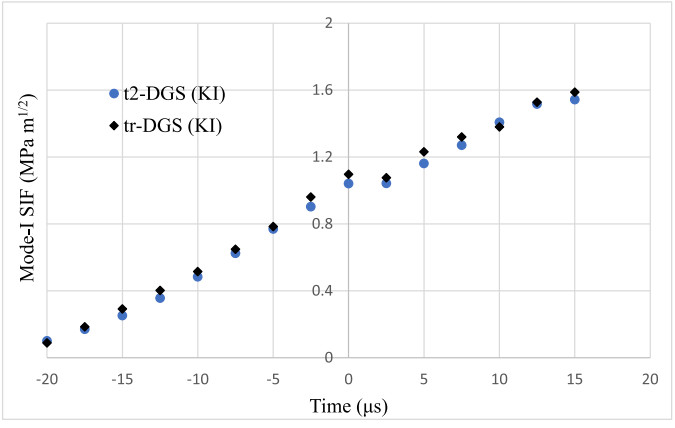

Fig. 10. Mode-I stress intensity factor histories measured by tr-DGS and t2-DGS methods.

tivity of tr-DGS relative to t2-DGS method. The values of ϕ_y measured by tr-DGS and t2-DGS in this quasi-static experiment were extracted to compare these two methods and verify the tr-DGS concept. In the region around the crack-tip, discrete angular deflection values of ϕ_y along the path $0.5 \le r/B \le 1.5$, $(\phi_y)_{tr-DGS}$ along $+45°$ and $+90°$, $(\phi_y)_{t2-DGS}$ along $-45°$ and $-90°$, were extracted. Unlike in the dynamic experiment, the rigid body motions cannot be neglected in the static counterparts. Therefore, the measurements were described as,

$$(\phi_y)_{measured} = (\phi_y)_{true} + C, \tag{15}$$

where C is the constant representing the rigid body motion, $(\phi_y)_{true}$ is the one devoid of rigid body motion. (The rigid rotation terms were found to be negligible and hence are not included here for clarity.) Using Eq. (15), an over-deterministic least-squares analysis was performed to determine C and remove the rigid body motion. Then, $(\phi_y)_{true}$ for tr-DGS and t2-DGS methods were used to find the ratio $\frac{(\phi_y)_{tr-DGS}}{(\phi_y)_{t2-DGS}}$, and is shown in Fig. 13. Again, the blue strip indicates the theoretical band from −1.57 to −1.32. It can be observed that the ratios are nearly con-

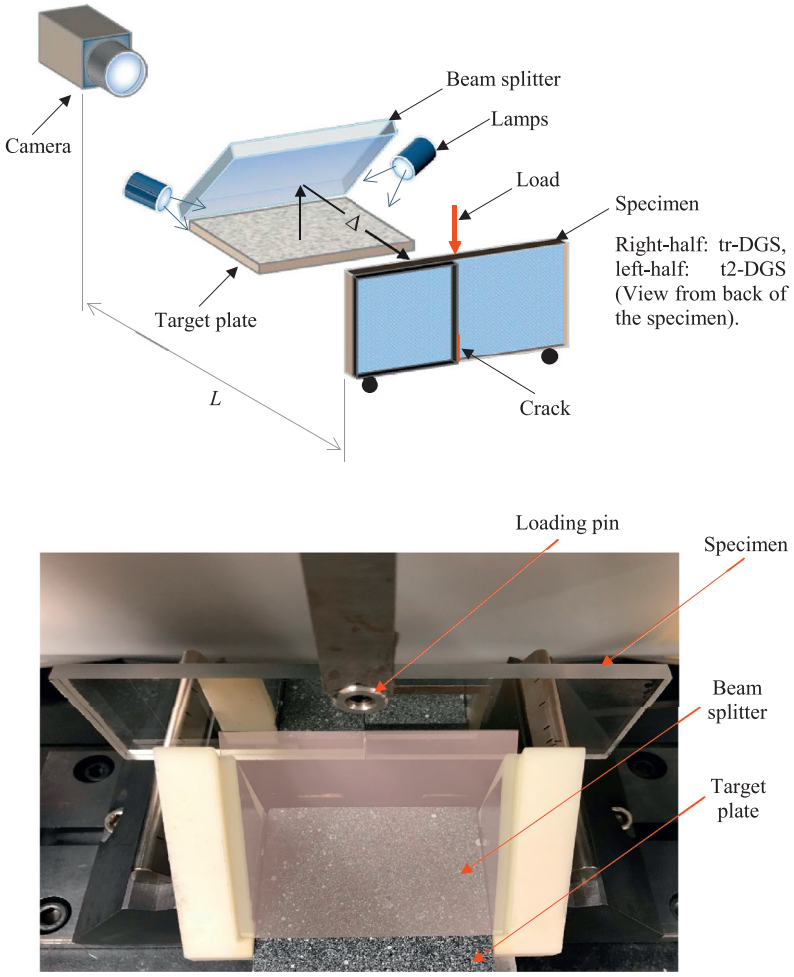

Fig. 11. Schematic of the experimental setup for static fracture study (*top*). Close-up view of the optical arrangement (*bottom*).

stant and are located close to if not on the blue strip, thus validating the predictions under quasi-static conditions also. During analysis, care was also exercised to locate the crack-tip from the contours.

5. Estimation of SIF from tr-DGS and t2-DGS methods

As a part of the family of DGS methods, these two approaches of tr-DGS and t2-DGS were used to measure the crack-tip stress intensity factors of PMMA beams under quasi-static symmetric 3-point bending. The measurements were also done using t-DGS and r-DGS methods separately for completeness. The experimental setup used is same as the one shown in Fig. 11. Rectangular PMMA specimens of dimensions 152 mm × 63.5 mm × 5.8 mm, with an initial crack of length 13 mm were used in each experiment for different DGS configurations. The other parameters of this experimental setup are same as the one used during verification of tr-DGS under quasi-static loading conditions, except the camera distance L was 1170 mm and Δ was 80 mm. All other experimental parameters were same for the four DGS methods. An 8-bit reference image was recorded with a resolution of 1504 × 1000 pixels before loading ($F = 0$ N). The speckle images were recorded at every 50 N increments up to a maximum load of 500 N. The images in the deformed state were correlated with the reference image as before. During image correlation, a sub-image size of 30 × 30 pixels (1 pixel = 37.86 μm) with 10 pixels overlap was used to extract the speckle displacements $\delta_{x:y}$ in the ROI. The displacement fields were then used to compute the two orthogonal angular deflection fields of light rays ($\phi_{x:y}$).

The angular deflection contour plots $\phi_{x:y}$ measured by these four DGS methods are plotted in Fig. 14 at the same load level of 500 N. It can be observed that the contours measured by t2-DGS and tr-DGS are visually larger and denser than those measured by the other two DGS methods, which indicates higher measurement sensitivity. Furthermore, tr-DGS is more sensitive than t2-DGS by comparison.

Based on Williams' asymptotic stress fields for mode-I cracks, the expressions for angular deflections for each of the DGS methods are given by [10,26],

$$(\phi_{x:y}) = D\frac{\partial(\sigma_{xx}+\sigma_{yy})}{\partial(x:y)} = D\sum_{N=1}^{\infty} A_N\left(\frac{N}{2}-1\right)r^{\left(\frac{N}{2}-2\right)}\begin{matrix}\cos\\ \sin\end{matrix}\left(\frac{N}{2}-2\right)\theta \quad (16)$$

where the constant D varies for each of the DGS methods: $D_{r-DGS} = (-\frac{\upsilon B}{E})$, $D_{t-DGS} = (C_\sigma B)$, $D_{t2-DGS} = (2C_\sigma B)$, and $D_{tr-DGS} = (2C_\sigma B - \frac{\upsilon B}{E})$. In the above equation, (r, θ) are the crack-tip polar coordinates and $A_1 = K_I\sqrt{\frac{2}{\pi}}$ with K_I being the mode-I stress intensity factor (SIF). In these experiments, ϕ_x data were used to evaluate SIFs by employing an overdeterministic regression analysis of measurements, and four higher order terms ($N = 4$) in Eq. (16). (The use of higher order terms also account for any rigid body motion issues when present.) Discrete angular deflections in the region around the crack-tip, $0.5 \le r/B \le 1.5$, $-135^\circ \le \theta \le 135^\circ$, were used in the regression analysis. This ensured that the data used was sufficiently close to the crack-tip, and also minimized the dominant triaxial effects near the crack-tip [10]. The results obtained are plotted in Fig. 15 for different load levels and measured by all the four DGS methods including tr-DGS and t2-DGS. For comparison,

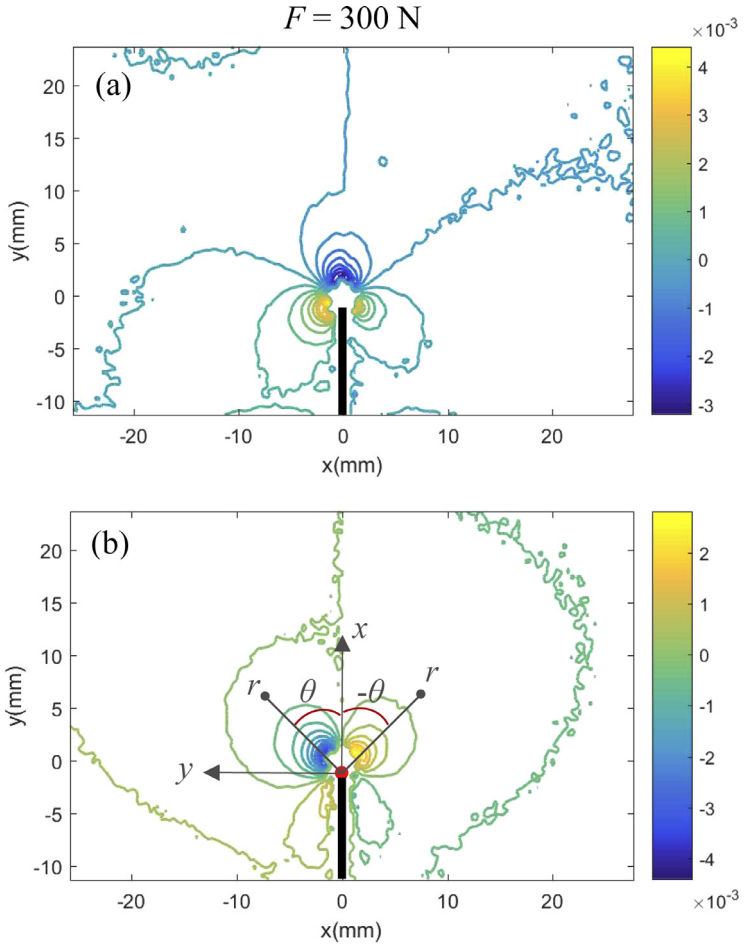

Fig. 12. Angular deflection contour plots proportional to stress gradients $(\sigma_x + \sigma_y)$: (a) ϕ_x; (b) ϕ_y. Contour increments = 4×10^{-4} rad.

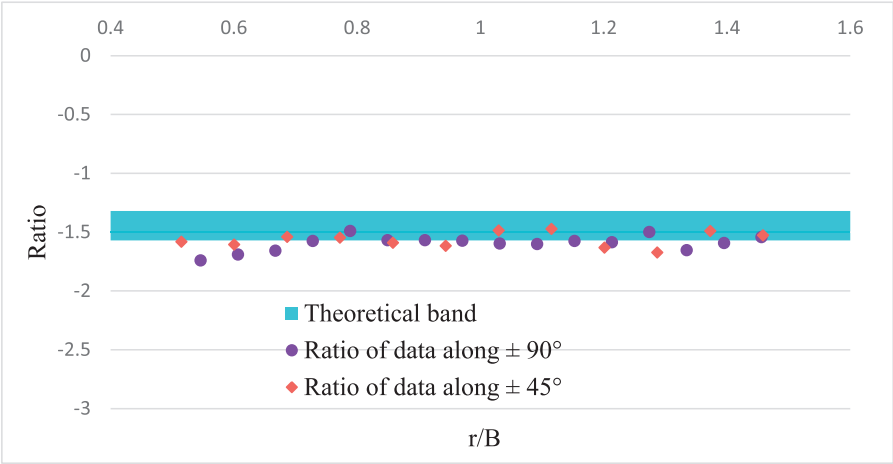

Fig. 13. Measured ratio of $\frac{(\phi_y)_{tr-DGS}}{(\phi_y)_{t2-DGS}}$ in $0.5 \le r/B \le 1.5$ along ±45° and ±90°.

the theoretical values of mode-I SIF were also calculated and plotted in Fig. 15 using [27]:

$$K_I = \frac{F \cdot S}{B \cdot W^{\frac{3}{2}}} \cdot \frac{3\left(\frac{a}{W}\right)^{\frac{1}{2}}\left[1.99 - \frac{a}{W}\left(1 - \frac{a}{W}\right)\left\{2.15 - 3.93\left(\frac{a}{W}\right) + 2.7\left(\frac{a}{W}\right)^2\right\}\right]}{2\left(1 + 2\frac{a}{W}\right)\left(1 - \frac{a}{W}\right)^{\frac{3}{2}}} \tag{17}$$

where F is the applied load, S is the span of the beam, a is the initial crack length, B is the specimen thickness, and W is the width. It is evident in Fig. 15 that there is a good agreement between the experimental and theoretical values of SIF, suggesting the feasible application of t2-DGS and tr-DGS for fracture mechanics investigations.

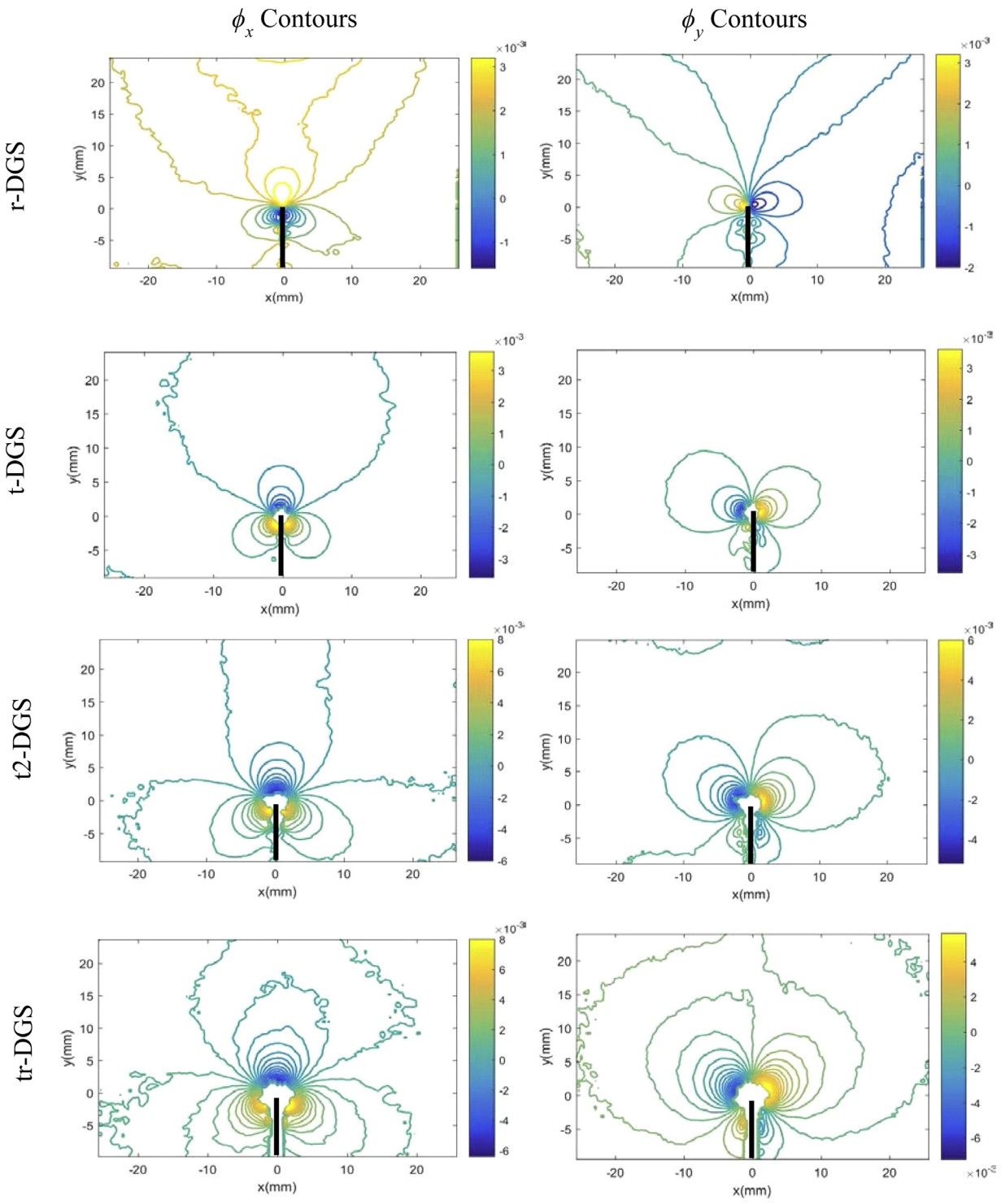

Fig. 14. Angular deflection contour plots of ϕ_x and ϕ_y for four DGS methods corresponding to load of 500 N. Contour increments = 4×10^{-4} rad.

6. Conclusions

In this paper, the concept and the feasibility of two new experimental configurations of Digital Gradient Sensing (DGS) methods with enhanced measurement sensitivity are described for experimental mechanics studies. The configurations are particularly valuable for studying high stiffness and low toughness substrates such as transparent ceramics. The concept identified as tr-DGS has measurement sensitivity that could be in excess of 3 relative to t-DGS. It exploits doubling of the optical path within the specimen besides reflection from the deformed back surface achieved by a reflective coating. When the deposition of a reflective coating is not feasible, a simple doubling of the optical path and hence the sensitivity over t-DGS can be achieved in t2-DGS configuration by using a detached reflector kept flush with the back surface of the specimen.

A dynamic mode-I crack initiation and growth experiment involving tr-DGS and t2-DGS measurements performed simultaneously on the same specimen above and below the crack line are comparatively ex-

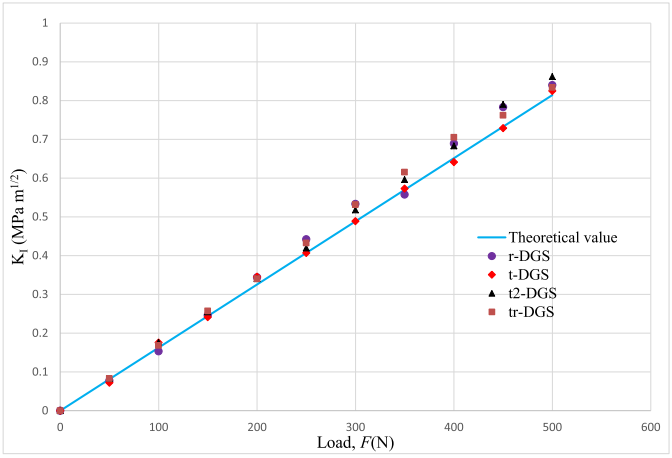

Fig. 15. Measured mode-I stress intensity factors (symbols) at different loads by different DGS methods. The solid line represents the corresponding theoretical values.

amined by exploiting the symmetry of the problem. The fact that the rigid body motion of speckles is negligible under stress wave loading conditions is taken advantage of using a single sensor ultrahigh-speed camera where reference and deformed speckle images are recorded only a few microseconds apart. The measured sensitivity ratio of angular deflections of light rays from tr-DGS and t2-DGS methods match well with those from predictions. A single edge notched beam bending experiment in a 3-point symmetric bending configuration is used to implement four different variants of DGS – t-DGS, r-DGS, t2-DGS and tr-DGS – to measure crack-tip stress gradient fields and extract mode-I SIF using Williams' asymptotic expressions. The measured SIF values match well with the theoretical predictions adding to the validation of the two new DGS configurations. Further implementation of t2-DGS and tr-DGS to study fast fracture of glasses and other transparent ceramics is planned.

Acknowledgments

Support for this research through Army Research Office grants W911NF-16-1-0093 and W911NF- 15-1-0357 (DURIP) are gratefully acknowledged.

Appendix-A

Estimation of lateral light ray shift in tr-DGS

A simplified 2D analysis for estimating the lateral shift of a generic light ray in tr-DGS method is attempted to supplement the ray diagram in Fig. 5 discussed earlier. Referring to Fig. A.1, an incident ray enters the *deformed* specimen (shaded in blue) at point '*a*' and refracts. Let the angles of incidence and refraction be θ_1 and θ_2, respectively, relative to the surface normal at '*a*'. To enable a geometric ray-optics based analysis, θ_1 – the local angle between the deformed and undeformed surfaces – is assumed to include the net influence of both the Poisson and stress-optic effects so that progressive bending of light rays through the medium can be avoided in the analysis since it would require *a priori* knowledge of the spatial distribution of stresses in the specimen. From Snell's law, $\frac{\sin\theta_1}{\sin\theta_2} = n$ where n is the locally averaged refractive index of the deformed body. Since θ_1 and θ_2 are small,

$$\theta_1 \approx n\theta_2. \tag{A1}$$

Next, the light ray *ab* reflects off point '*b*' on the rear *deformed* surface of the specimen as *bc* such that the angles of incidence and reflection are θ_3. As noted earlier, in reality, light rays bend progressively when

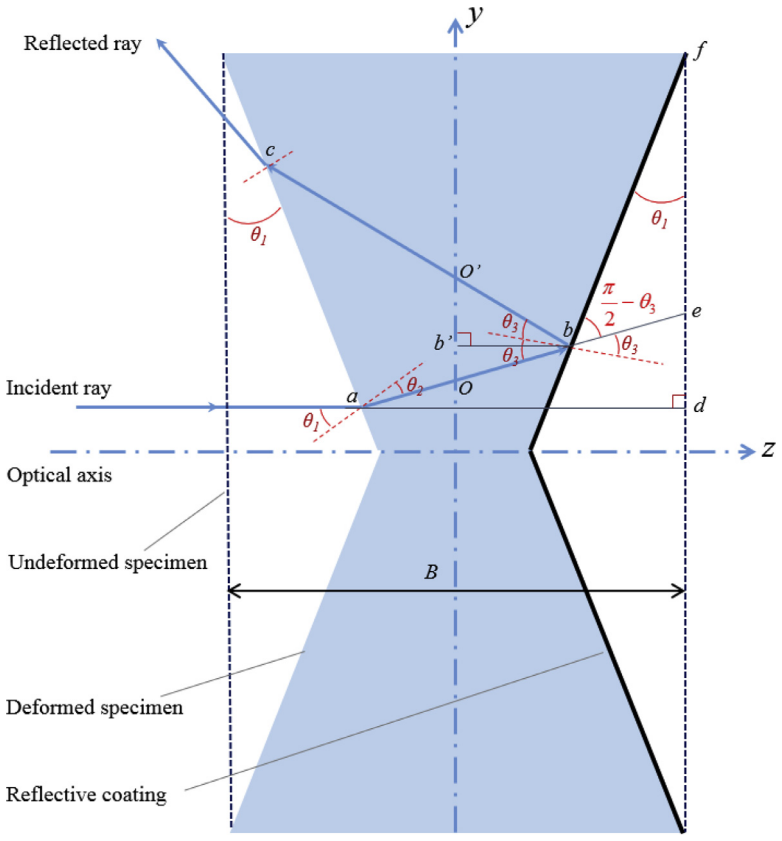

Fig. A.1. Exaggerated light ray diagram for tr-DGS.

traveling in specimen and are again assumed to be straight lines for estimation purposes.

The incident ray is extended to '*d*' so that *ad* is perpendicular to the undeformed rear surface (dark blue dotted line) of the specimen. The ray *ab* is also extended beyond '*b*' to '*e*' to the undeformed rear surface. Let '*f*' represent a generic specimen location where the Poisson deformation is zero or negligible. Now, it can be observed that $\angle ead = \theta_1 - \theta_2$, $\angle bfe = \theta_1$ and $\angle fbe = \frac{\pi}{2} - \theta_3$. Hence, $\angle aed = \angle fbe + \angle bfe = \frac{\pi}{2} - \theta_3 + \theta_1$. Further, it can be observed that Δaed is a right angled triangle and hence, $\angle ead + \angle aed = \frac{\pi}{2}$, or, $\theta_1 - \theta_2 + \frac{\pi}{2} - \theta_3 + \theta_1 = \frac{\pi}{2}$, and hence

$$2\theta_1 = \theta_2 + \theta_3. \tag{A2}$$

In $\Delta O'bO$, bb' is normal to OO', $\angle O'bO = 2\theta_3$, $\angle b'bO = \angle ead = \theta_1 - \theta_2$, $\angle b'bO' = 2\theta_3 - (\theta_1 - \theta_2)$. Hence,

$(O'b') = (b'b)\tan(2\theta_3 - \theta_1 + \theta_2) \approx (b'b)(2\theta_3 - \theta_1 + \theta_2)$, and

$(Ob') = (b'b)\tan(\theta_1 - \theta_2) \approx (b'b)(\theta_1 - \theta_2)$ for small angles. Therefore,

$$OO' = Ob' + O'b' = 2(b'b)\,\theta_3. \tag{A3}$$

Based on Eq. (A1) and (A2), $\theta_3 = (2 - \frac{1}{n})\theta_1$. Also, note that $0 \le 2(b'b) \le B$, where B is the undeformed thickness of the specimen. Hence, the approx. value of OO' at a generic position can be expressed as,

$$0 \le OO' \le (2 - \frac{1}{n})B\theta_1. \tag{A4}$$

For PMMA, assuming $n \approx 1.5$, B to be of the $O(10^{-3})$ m, and θ_1 to be of the $O(10^{-3})$ radians, the largest value of OO' would be of the $O(10^{-6})$ m. Hence the lateral shift OO' in tr-DGS could be neglected relative to a typical sub-image to sub-image distance of less than $O(10^{-3})$ m. Extending similar arguments to t2-DGS, the lateral shift of OO' can also be neglected since t2-DGS is less sensitive than tr-DGS.

References

[1] Periasamy C, Tippur HV. A full-field reflection-mode digital gradient sensing method for measuring orthogonal slopes and curvatures of thin structures. Meas Sci Technol 2013;24:025202.

[2] Periasamy C, Tippur HV. Full-field digital gradient sensing method for evaluating stress gradients in transparent solids. Appl Opt 2012;51(12):2088–97.

[3] Grujicic M, Bell WC, Pandurangan B. Design and material selection guidelines and strategies for transparent armor systems. Mater Des 2012;34:808–19.

[4] Patel PJ, Gilde GA, Dehmer PG, McCauley JW. Transparent armor. AMPTIAC Newsl 2000;4(Fall):1–16.

[5] Straßburger E. Ballistic testing of transparent armour ceramics. J Eur Ceram Soc 2009;29(2):267–73.

[6] Dally JW. Dynamic photoelastic studies of fracture. Exp Mech 1979;19(10):349–61.

[7] Parameswaran V, Shukla A. Dynamic fracture of a functionally gradient material having discrete property variation. J Mater Sci 1998;33(13):3303–11.

[8] Lee J, Kokaly MT, Kobayashi AS. Dynamic ductile fracture of aluminum SEN specimens an experimental-numerical analysis. Int J Fract 1998;93:39–50.

[9] Tippur HV. Coherent gradient sensing: a Fourier optics analysis and applications to fracture. Appl Opt 1992;31:4428–39.

[10] Tippur HV, Krishnaswamy S, Rosakis AJ. Optical mapping of crack tip deformations using the methods of transmission and reflection coherent gradient sensing: a study of crack tip K-dominance. Int J Fract 1991;52:91–117.

[11] Tippur HV. Simultaneous and real-time measurement of slpoe and curvature fringes in thin structures using shearing interferometry. Opt Eng 2004;43:3014–20.

[12] Ma K, Xie H. Spatially-phase-shifted coherent gradient sensor for full-field measurement of surface slope and curvature. Exp Mech 2016;56:1073–82.

[13] Ma K, Xie H. A novel phase shifting technique of coherent gradient sensing method for measuring crack-tip K-dominance. Exp Mech 2017;57:1239–48.

[14] Chen DJ, Chiang FP, Tan YS, Don HS. Digital speckle-displacement measurement using a complex spectrum method. Appl Opt 1993;32(11):1839–49.

[15] Chu TC, Ranson WF, Sutton MA, Peters WH. Application of digital image correlation techniques to experimental mechanics. Exp Mech 1985;25(3):232–44.

[16] Sutton MA, Orteu JJ. Image correlation for shape, motion and deformation measurements. New York, NY, USA: Springer; 2009.

[17] Pankow M, Justusson B, Waas AM. Three-dimensional digital image correlation technique using single high-speed camera for measuring large out-of-plane displacements at high framing rates. Appl Opt 2010;49:3418–27.

[18] Periasamy C, Tippur HV. Measurement of orthogonal stress gradients due to impact load on a transparent sheet using digital gradient sensing method. Exp Mech 2013;53:97–111.

[19] Miao C, Sundaram BM, Huang L, Tippur HV. Surface profile and stress field evaluation using digital gradient sensing method. Meas Sci Technol 2016;27:095203.

[20] Zhang C, Qu Z, Fang X, Feng X, Hwang KC. Digital gradient sensing method to evaluate thermal stress at elevated temperatures. Exp Mech 2016;56:1123–32.

[21] Sundaram BM, Tippur HV. Full-field measurement of contact-point and crack-tip deformations in soda-lime glass. Part-I: quasi-static loading. Int J Appl Glass Sci 2018;9:114–22.

[22] Sundaram BM, Tippur HV. Full-field measurement of contact-point and crack-tip deformations in soda-lime glass. Part-II: stress wave loading. Int J Appl Glass Sci 2018;9:123–36.

[23] Tippur HV. Optical techniques in dynamic fracture mechanics. Dynamic fracture mechanics. World Scientific Publications; 2006.

[24] Dally JW, Riley WF. Experimental Stress Analysis. 4th ed., College House Enterprises, 2005.

[25] Xu L, Tippur H, Rousseau C-E. Measurement of contact stresses using real-time shearing interferometry. Opt Eng 1999;38:1932–7.

[26] Williams ML, Calif P. On the stress distribution at the base of a stationary crack. J Appl Mech 1959;vol. 24:109–14.

[27] Janssen M, Zuidema J, Wanhill R. Fracture mechanics. 2nd ed. VSSD; 2006.